Article

Band Gap Narrowing in Lead-Halide Perovskites by Dynamic Defect Self-Doping for Enhanced Light Absorption and Energy Upconversion

Yongliang Shi, Weibin Chu,* Lili Zhang, Bipeng Wang, Wissam A. Saidi, Jin Zhao, and Oleg V. Prezhdo*

Read Online

ACCESS | Metrics & More | Article Recommendations | SI Supporting Information

ABSTRACT: Metal halide perovskites (MHP) have attracted great attention in the photovoltaic industry due to their high and rapidly rising power conversion efficiencies, currently over 25%. However, hybrid organic−inorganic MHPs are inherently chemically unstable, limiting their application. All-inorganic MHPs perovskites, such as $CsPbI_3$, have many merits, but their stable conversion efficiency is lower, around 18%, due to a larger band gap causing a mismatch with the solar spectrum. Choosing α-$CsPbI_3$ as a prototypical system, we demonstrate a new general concept of dynamic defects that fluctuate between deep and shallow states, and increase the range of absorbed solar photons, without accelerating the nonradiative electron−hole recombination. In their deeper energy state, the defects narrow the band gap and allow the harvesting of light with longer wavelengths. Fluctuating to shallower energies, the defects allow the escape of photogenerated charges into bands, enabling charge transport and resulting in the defect-mediated upconversion of thermal energy into electricity. Defect covalency and participation of low-frequency anharmonic vibrations decouple trapped charges from free charge carriers, minimizing nonradiative charge carrier losses. Our findings demonstrate that defect covalency and defect dynamics are unique and important properties of MHPs, and can be used to optimize MHPs for efficient solar energy harvesting and optoelectronic applications.
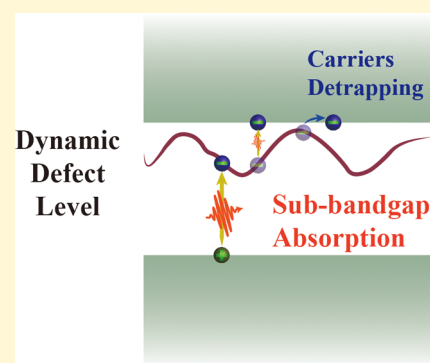
INTRODUCTION

Metal halide perovskites (MHPs) based solar energy technologies have advanced substantially in the photovoltaic community.[1−12] The certified power conversion efficiency (PCE) of perovskite solar cells has rapidly exceeded 25% over the past decade, surpassing both traditional and emerging solar cells.[13] Despite the undoubted success of the MHP solar cells, long-term stability is still a significant obstacle to the commercialization of hybrid organic−inorganic perovskites due to potential volatility and degradation of the organic cations.[14−16] Motivated by this point of view, all-inorganic perovskites without reactive organic components have appeared as promising alternatives with better stability.[17−20] In particular, inorganic cesium lead halide perovskites have gained broad attention due to comparable optoelectronic properties with their organic analogs.[21−23] For example, $CsPbI_3$ is highly optically active in the ultraviolet−visible (UV−vis) region of the solar spectrum. Recently, solar cells based on black α-$CsPbI_3$ and β-$CsPbI_3$ reached a stable PCE of 17%[19] and over 18%,[12,24−26] respectively. However, due to its larger bandgaps (∼1.7 eV), the PCEs of $CsPbI_3$ solar cells still lag behind those of their organic counterparts.

According to the Shockley−Queisser (SQ) theory for single-junction solar cells,[27] the theoretical PCE limit of $CsPbI_3$ solar cells is only ∼28%,[28] which is appreciably inferior to 30−33% for solar absorbers with bandgaps in the 1.2−1.6 eV range.

Thus, bandgap engineering of $CsPbI_3$ is a potential route to further improve the PCE. In general, defect and dopant engineering is a meaningful way to adjust the bandgap. In a traditional semiconductor, defects narrow the bandgap by introducing deep defect states. At the same time, these defect states vastly accelerate the electron−hole recombination via the Shockley−Read−Hall (SRH) process[29] and consequently suppress the PCE by converting the electronic energy of photon-excited carriers to phonons. Intriguingly, MHPs possess high defect tolerance due to their soft nature and strong defect covalency, illustrated by our previous works.[30−34] Based on these studies, we introduce a new concept that some intrinsic defects in MHPs are generally not determinantal for nonradiative charge recombination. Hence, self-doping defect engineering will be ideal for narrowing the bandgap without introducing extra efficiency loss from nonradiative electron−hole (*e-h*) recombination. Implementation of this concept in practice requires a comprehensive understanding of defect electronic properties and defects induced sub-bandgap
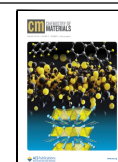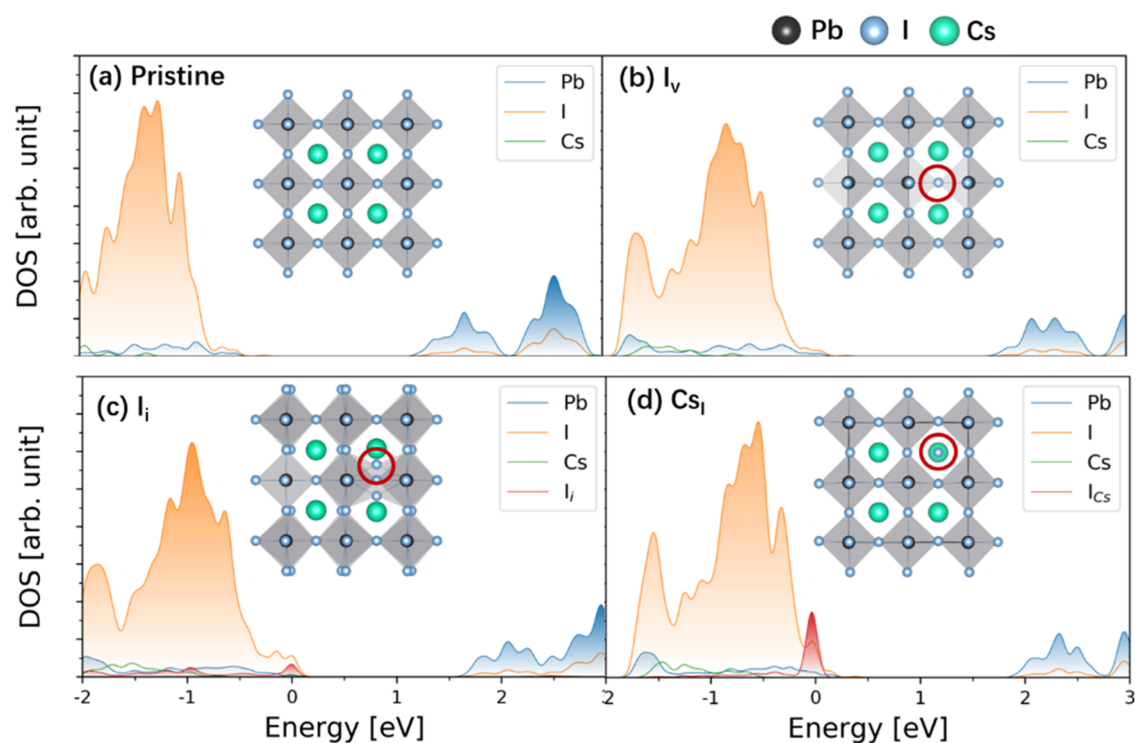
Figure 1. Atom-projected DOS for pristine and defective α-CsPbI$_3$ at 0 K. The energy reference is put at the Fermi level. The insets show atomic structures, with the red circles indicating the defect locations. The defects introduce shallow trap states near the band edges at 0 K.

absorption, which can be characterized by time domain atomistic calculations.

This work puts forth a new general concept—covalent dynamic defect self-doping—to overcome the critical bottleneck in the photovoltaic performance of all-inorganic perovskites and to enable upconversion of thermal energy into electricity. The concept is demonstrated quantitatively using ab initio nonadiabatic molecular dynamics (NAMD) and real-time photoabsorbance calculations, focusing on bandgap narrowing and its influence on the *e-h* recombination. Several native defects in all-inorganic perovskites can form strong covalent bonds and new stable chemical species at ambient conditions. Notably, the covalency nature of MHPs and their peculiar anharmonic lattice introduce native dynamic defects, which fluctuate between deep and shallow levels inside the bandgap. Dynamic defects combine the merit of deep defects that enhance the sub-bandgap light-harvesting over a broad energy spectrum and the merit of shallow defects that transiently trap charge carriers and allow the carriers to escape thermally from the trapped states and retain carrier mobility, upconverting thermal energy to current. Furthermore, although deep trap levels do exist in MHPs, the dynamic defects have minor influence on the *e-h* recombination due to the decoupling of the trapped and complementary free charges, and because only low-frequency phonons interact with the carriers generating weak charge-phonon coupling. The deep levels can act as sub-bandgap photoabsorption centers, which enable utilization of two sub-bandgap photons sequentially. Control of the defect-assisted *e-h* recombination can allow one to use dynamic defects for the engineering of intermediate band (IB) solar cells, which can surpass the SQ efficiency limit.[35] Our results pave the way to the optimization of light absorption and nonradiative *e-h* recombination in wide bandgap MHP solar cells and other optoelectronic devices.

RESULTS

To examine the general concept of covalent defect self-doping, we take α-CsPbI$_3$ as a prototypical system. The cubic phase of CsPbI$_3$ is less stable than the orthorhombic perovskite polymorph[36] and can be stabilized in perovskite nanocrystals with a suitable choice of ligands.[37] We focus on three intrinsic defects possibly with strong covalency, namely, I vacancy (I$_V$), I interstitial (I$_i$), and Cs substituted by I (Cs$_I$). These defects have low formation energies among the three kinds of vacancy defects (I$_V$, Pb$_V$, Cs$_V$), the three interstitial defects (I$_i$, Cs$_i$, Pb$_i$), and the six antisite defects (I$_{Cs}$, Cs$_I$, Pb$_I$, I$_{Pb}$, Pb$_{Cs}$, Cs$_{Pb}$, where A$_B$ indicates that A is substituted by B).[38−40] In the following, we start the discussion with geometric structure and static electron properties at 0 K. Then, we consider the thermal impact on pristine and defective α-CsPbI$_3$ through electron−phonon interactions. Third, we investigate the nonradiative *e-h* recombination process. Finally, we close with the discussion on the dynamic defect enhanced sub-bandgap light absorption.

Static Electronic Structure. It is instructive to study the static (0 K) electronic structure of α-CsPbI$_3$ with and without defects before performing a comprehensive *e-h* recombination dynamics simulation. Figure 1 shows the atom-projected density of states (DOS) of the I$_V$, I$_i$, and Cs$_I$ defect systems, with the corresponding optimized configurations shown in the insets. For comparison, we also present the results for the pristine system. Despite the strong and distinct nature of the defects, all the introduced defect states are shallow and are close to the band edges at 0 K. We consider a defect state in the bandgap to be shallow, if the trapped carrier can be released by thermal excitation. Otherwise, the defect is deep. In the static limit, I$_V$ is a shallow electron acceptor and introduces a shallow defect state near the conduction band minimum (CBM). In comparison, I$_i$ is a shallow electron donor and introduces shallow defect states near the valence band
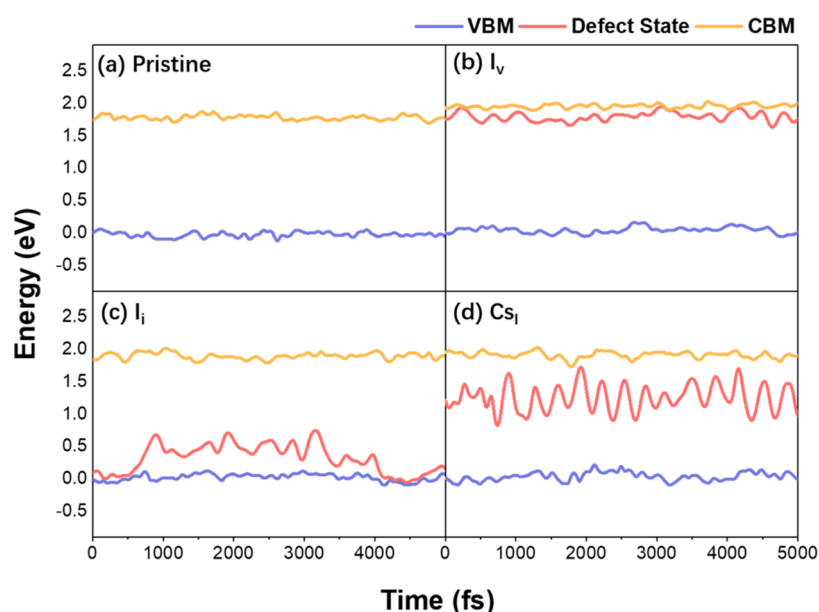
Figure 2. Evolution of the VBM, CBM and defect levels in the α-CsPbI$_3$ systems at 300 K. The energy reference is put at the VBM of the initial configuration. I$_i$ (c) and Cs$_I$ (d) exhibit an oscillatory behavior between shallow and deep states at 300 K.

maximum (VBM). The electronic characters of I$_V$ and I$_i$ are general in other types of MHP.[31,41] Cs$_I$, i.e., the original Cs atom substituted by an I atom, introduces a shallow defect state near the VBM. Note that its organic counterpart is different. Specifically, the MA$_I$ defect in MAPbI$_3$ (the counterpart of Cs$_I$ in CsPbI$_3$) introduces a deep defect state located 1.4 eV above the VBM due to the formation of the iodine trimer.[31] The calculated electronic properties of these defects are consistent with the previous study.[38] Shallow defect states usually bring negligible perturbation to the electronic structure of the host system. Hence, these defects are not expected to optimize the bandgap of α-CsPbI$_3$. However, it is evident that static simulations based on lattice configurations in 0 K equilibrium are inappropriate for interpreting the dynamical features of MHPs, as the thermal impact is crucial to defect level and *e-h* recombination.[42]

Thermally Activated Dynamic Defect. Due to the soft nature of MHPs, considerable thermal vibrations in defective α-CsPbI$_3$ at ambient temperature have a significant impact on the electronic structure, hence, invoking electron−phonon interactions. Figure 2 shows the time evolution of the frontier and defect energy levels at 300 K. Under ambient temperature, only I$_v$ remains a shallow defect state near the CBM, while the defect states in I$_i$ and Cs$_I$ exhibit large fluctuations, showing an oscillatory behavior between shallow and deep states (Figure 2c,d). Therefore, we refer to I$_i$ and Cs$_I$ as dynamic defects. Moreover, I$_i$ and Cs$_I$ lift up the defect levels to ~0.3 and 1.3 eV above the VBM, respectively, with a canonical average at the ambient temperature. The significant lifting of the defect level is rationalized with the formation of an iodine trimer as proposed in the previous study.[30,31,43] For Cs$_I$, the level lifting is so large that it becomes closer to the CBM than the VBM. The defect level of the I$_3$ species has been shown to depends on the strength of its covalent bond.[43] To evaluate the self-interaction error of the Perdew−Burke−Ernzerhof (PBE) functional and the importance of spin−orbit coupling (SOC), we further perform an molecular dynamics (MD) simulation of Cs$_I$ using the HSE06 hybrid functional with consideration of SOC. The oscillation of the defect state level between the

shallow and deep states is still observed (Figure S1a). We also test the results with respect to the simulation cell size. The behavior of the Cs$_I$ defect level obtained with the 8-times larger $2\sqrt{2} \times 2\sqrt{2} \times 4$ supercell (Figure S1b) confirms the behavior seen in Figure 2d.

The combination of strong covalency, charge localization and large anharmonicity of MHPs gives rise to these dynamic defects undergoing significant defect energy level fluctuations and lifting. I$_i$ and Cs$_I$ oscillate with the amplitudes of ~0.8 and 0.9 eV. It indicates that the dynamic defect levels of I$_i$ and Cs$_I$ are sensitive to the type and position of the defect iodine atom, in particular, the formation of an iodine dimer or an iodine trimer, which will significantly alter the localization of the defect electronic distribution. The large anharmonicity of MHPs, resulting from the relatively flat potential energy surfaces,[44] enhances the vibrational amplitude of these dynamic defects. Further, the dynamic lifting of the shallow defects located just above the VBM at 0 K results from strong covalency. Agiorgousis et al. have argued that strong covalency between homoions, such as two Pb^{2+} and three I$^-$ leading to a Pb^{2+} dimer and an I$^-$ trimer, results in deep energy levels.[43] The strong covalency of the I$_i$ and Cs$_I$ defects in CsPbI$_3$ rationalizes their dynamic character. I$_i$ and Cs$_I$ oscillate between shallow and deep states depending on whether an I dimer and an I trimer are formed or not. Remarkably, the defect level of Cs$_I$ lifts so considerably that it becomes closer to the CBM than the VBM at the ambient temperature, which is similar to what we have found in other MHPs.[30,31] This can be rationalized by the stronger bonding in the iodine trimer of the Cs$_I$ system compared with I$_i$. In contrast, for I$_V$, we did not observe deep energy levels in long-time MD simulation due to the high formation energy of a Pb^{2+} dimer.[43] According to the simple Shockley−Read−Hall (SRH) model,[29] deep transition levels introduced by strong covalency can be harmful recombination centers and carry the critical consequence of the solar cell performance loss. As we showed in the previous study,[30] though strong covalency introduces the new deep level, the strong covalency also constrains the defect state electron density to a small space with weak coupling to the
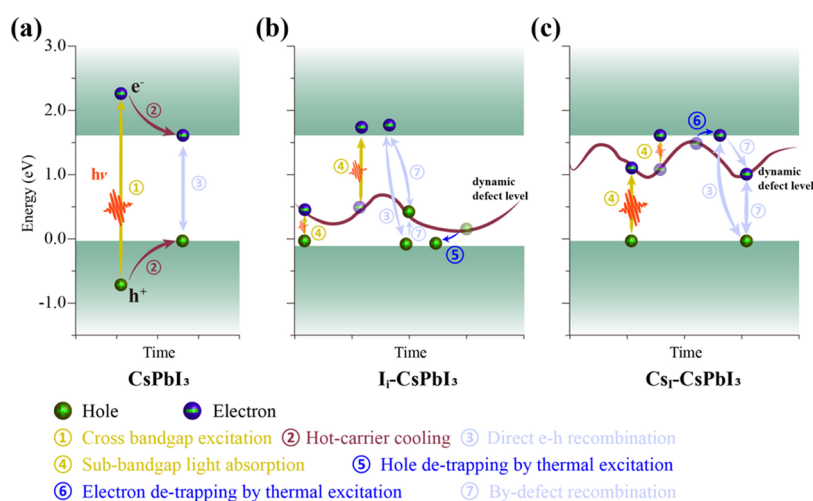
Figure 3. Comprehensive schematic of the photophysical processes. (a) Pristine α-CsPbI$_3$, (b) Cs$_I$, and (c) I$_i$. For the dynamic defect, when the defect level is shallow, thermal excitation can promote carrier detrapping into the band. When the energy of the same defect level is deep, it creates sub-bandgap excitation and extends light absorption into longer wavelengths.
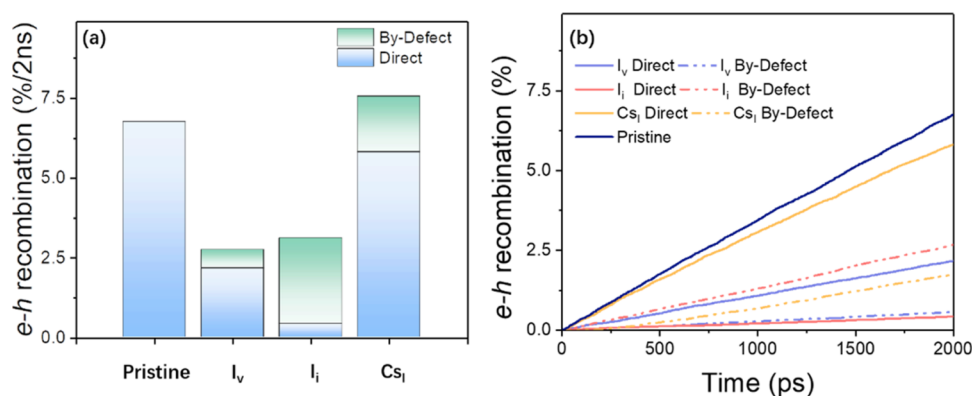
Figure 4. e-h recombination process in the α-CsPbI$_3$ systems. (a) e-h recombined percentage after two ns. The direct and by-defect e-h recombined percentages are shown by the blue and green color bars. (b) The time-dependent e-h recombined percentage for different systems. The direct and by-defect e-h recombined percentages are shown with the solid and dash lines, respectively.

frontier orbital, thus suppressing the e-h recombination. Importantly, the dynamic defect narrowing of the bandgap can be utilized to enhance the solar light harvesting. In the following section, we show that the combination of these dynamic defects improves light harvesting by a distinct mechanism.

**Nonradiative Electron–Hole Recombination Process.** The nonradiative electron–hole recombination dissipates the electronic energy into heat and is the dominant mechanism of energy losses in solar cells. Figure 3a depicts the photo-excitation, and subsequent hot-carrier cooling and e-h recombination processes. These processes are indicated with 1−3 in Figure 3, and occur in both pristine and defective α-CsPbI$_3$. It is to be noted that a sub-bandgap photon is unexploited in the pristine α-CsPbI$_3$. However, for defective α-CsPbI$_3$, the sub-bandgap photon can be utilized to extend the absorbance. The pathways of the photoexcited electrons are complex, as they usually evolve multiple states and processes, including hot-carrier charge cooling, trapping and detrapping, photon absorption, and e-h recombination, as illustrated in Figure 3b,c. In addition, carrier–carrier scattering is possible at high carrier densities, resulting in Auger-assisted carrier trapping, recombination and re-excitation. High light intensity can lead to re-excitation of free or trapped carriers by photons.

In addition to the common above-the-bandgap excitation, sub-bandgap photons can be absorbed to promote an electron from VB to empty defect states or from filled defect states to CB, process 4 in Figure 3b,c. The dynamic nature of these defects brings the electron to a higher or lower energy as the defect level fluctuates due to adiabatic electron–phonon interactions, i.e., without transitions between electronic states. When the defect levels fluctuate between shallow and deep configurations, they harvest sub-bandgap photons over a relatively broad energy range due to transitions between band edges and the intermediate levels. Further, when the fluctuation of the dynamic defect level brings the carrier to a shallow state within a few k_BT of thermal energy near a band edge, thermal excitation promotes the carrier detrapping to a band, and therefore, the trapped carrier becomes a free carrier to further improve the PCE, as illustrated in Figure 3b,c (processes 5 and 6). Nevertheless, the nonradiative e-h recombination (processes 3 and 7) can deteriorate the efficiency of the solar cell if such dynamic defects form strong recombination centers. The aforementioned dynamic defects significantly impact the optical and dynamic properties of α-CsPbI$_3$ due to the large-amplitude oscillation of the defect states inside the fundamental bandgap. Consequently, it is important to study trap-assisted charge recombination, which

Table 1. Canonically Averaged Absolute Values of NAC and Pure-Dephasing Times between Pairs of the VBM, CBM, and Defect States[a]

	NAC (meV)			pure dephasing time (fs)		
	VBM-CBM	VBM-defect	CBM-defect	VBM-CBM	VBM-defect	CBM-defect
pristine	0.41			10.1		
I_v	0.43	0.28	0.26	11.3	8.1	9.6
I_i	0.30	2.86	0.23	8.6	3.5	3.4
Cs_I	0.35	0.19	0.76	8.6	3.3	3.5

[a]Defect assisted recombination is a two-step process. Charge trapping by the defects is fast, because the corresponding NAC is large. However, the subsequent recombination is slow, because the corresponding NAC is small.
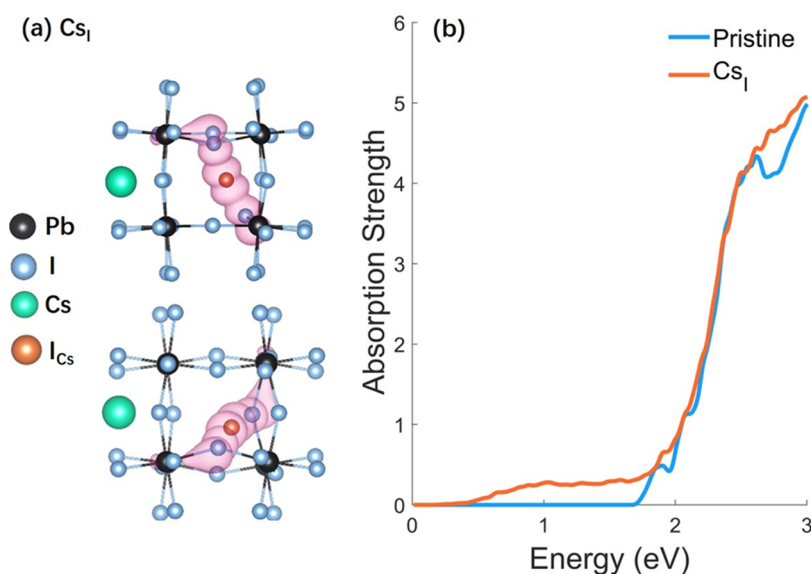
Figure 5. Dynamic defect enhanced optical absorption. (a) Different views of the spatial distribution of the trap state density in Cs_I. (b) Optical absorption of pristine α-CsPbI$_3$ and α-CsPbI$_3$ with the Cs_I defect. The absorption of the Cs_I system is extended into the red region of the visible spectrum. Both the charge densities and the spectra are calculated by canonical ensemble averaging over 7000 configurations.

can be performed rigorously by the real-time ab initio calculation. Therefore, we model the energy loss pathways (processes 3 and 7) using the NAMD framework within the decoherence-induced surface hopping (DISH) scheme.[45,46] Thermal excitation and relaxation are intrinsically included in the surface hopping scheme. Radiative and Auger e-h recombination processes are not discussed in this work because radiative recombination is significantly slower than trap-assisted recombination, and since Auger processes require high light intensity and carrier density.

To provide a comprehensive picture of the energy loss processes, Figure 4a presents the direct and by-defect contributions to the nonradiative charge recombination after 2 ns. The height of the bar component of the corresponding color gives the probability, in percent, that a particular pathway has occurred within 2 ns after the photoexcitation. Figure 4b illustrates the time-evolution of the direct and by-defect recombination in the pristine and defective systems, with the slopes of the lines providing the rates. For the pristine system, we found that ≈6.8% of the nonradiative recombination occurs within 2 ns, with an estimated e-h lifetime of 30 ns. In addition to the desired slow e-h recombination in the pristine system, α-CsPbI$_3$ shows defect tolerance comparative with MAPbI$_3$ and β-CsPbI$_3$. In the previous studies, we found that the e-h recombination will not be accelerated significantly and can even be suppressed by some intrinsic defects.[30,31] The total 2 ns recombination probabilities are found to be ≈2.7% (I_v),

≈3.1% (I_i), ≈7.6% (Cs_I), corresponding to the lifetimes of ≈73 ns (I_v), ≈ 64 ns (I_i), ≈ 27 ns (Cs_I), respectively. I_i and I_v suppress the recombination rate by a factor of ≈2, while Cs_I does not affect the recombination rate too appreciably. In common, slower e-h recombination reduces electronic energy dissipation into heat, and hence, enhances the overall PCE.

The e-h recombination rates obtained in NAMD simulations are strongly dependent on the energy gap, decoherence rate, and NA coupling (NAC) between the initial, intermediate, and final states.[47−51] Typically, a weaker NAC, a larger energy gap, and a faster decoherence lead to slower e-h recombination. The defect states, especially deep defects, have narrower energy gaps to the band edges compared to the fundamental bandgap, usually leading to more significant and detrimental e-h recombination. At the same time, generally to MHPs, deep defect states are spatially localized, possessing a weaker NAC and a faster decoherence due to reduced spatial overlap and weaker correlation with the band edge states, and that may counteract the drawback of a narrower energy gap due to the presence of defects.

The strength of NAC, d_{jk} determines the probability of hopping between electronic states. The scalar form of the NAC has the units of energy and reads

$$d_{jk} = i\hbar \langle \varphi_j | \frac{\partial}{\partial t} | \varphi_k \rangle = i\hbar \frac{\langle \varphi_j | \nabla_R H | \varphi_k \rangle}{\varepsilon_j - \varepsilon_k} \dot{R} \quad (1)$$

Here, H is the Kohn−Sham (KS) Hamiltonian, φ_j, φ_k, ε_j and ε_k are, respectively, the wave functions and eigenvalues for the initial and final states j and k, and $\dot{R}$ is the nuclear velocity. The middle part of eq 1 shows that the NAC is determined by the time differential of two orbitals' overlap, and we compute NACs numerically as the overlap of two orbitals at adjacent ionic time steps along the MD trajectory. The righthand-side shows that the NAC is directly proportional to the electron−phonon coupling term $\langle \varphi_j | \nabla_R H | \varphi_k \rangle$ and the nuclear velocity $\dot{R}$, and that it is inversely proportional to the energy difference ε_j-ε_k. Since the NAC varies with atomic configuration along the trajectory, we report in Table 1 the canonically averaged absolute value of the NAC between the relevant states to quantify the coupling strength for the systems under investigation.

The presence of defects perturbs the VBM and CBM orbitals. As shown in Figure S2, the VBM partial charge density in I_v and I_i is repulsed from the defect site, while the CBM remains delocalized. As a result, the VBM-CBM overlap decreases, and the VBM-CBM NAC diminishes in the defective systems, as shown in Table 1. The diminished NAC between the frontier orbitals indicates that the recombination through the direct pathway is prolonged.

Electron−phonon interaction plays a central role in the nonadiabatic e-h recombination dynamics. First, the strength of the electron−phonon interaction is proportional to the overlap between the two corresponding orbitals. Figure S2 shows the partial charge densities of the frontier orbitals and the defect states for representative configurations extracted from the MD trajectories. They are consistent with the projected DOS given in Figure 1. The VBM and CBM charge densities are delocalized over I and Pb atoms uniformly in the pristine system, giving the NAC of 0.41 meV (Table 1). The defects perturb both orbitals significantly due to strong distortions in the lattice. Despite the ionic nature of MHPs, the formation of the iodine trimer indicates its strong covalency. Figure 5a shows canonically averaged electron densities of the defect states. The covalent bond localizes the electron distributions strongly, which leads to a weak overlap of the defect states with the lattice, rationalizing the small NAC values for the transition involving the defect states, Table 1. Second, the adiabatic electron−phonon interaction drives fluctuation of the energy levels and causes rapid decoherence of the electronic states superpositions formed during the transitions. Generally, a larger energy gap fluctuation and a more rapid correlation decay result in a faster decoherence.[52] As shown in Figure 2, the fluctuation amplitude of the energy gap between the defect levels and the VBM/CBM levels is much more significant in I_i and Cs_I than in I_V. This explains the shorter decoherence time in I_i and Cs_I than in I_v. Third, not all phonons contribute equally to the NAC. Figure S3 shows Fourier transforms of the autocorrection functions of the energy levels. Phonons coupled with the VBM, CBM, and defect states are low frequency, around 120 cm^{-1} and less. These phonons arise from the motions of the heavy inorganic Pb−I frameworks.[53] These low-frequency phonons have small nuclear velocities, hence, leading to a weak NAC.

Although the carrier traps generated by the covalency defects are not notably harmful to the recombination lifetime, they potentially diminish carrier mobility by inducing carrier scattering from the defects. For instance, trap states can suppress the device's performance by preventing carriers from reaching the carrier extraction layers.[54] Carrier detrapping and

escape back to the band edges play a vital role in avoiding operational electronic mobility loss. Intriguingly, compared to the traditional deep defects, the dynamic defects offer an efficient thermal detrapping pathway operating when the defect state level approaches the band edge, process 5 (hole carrier) and process 6 (electron carrier) in Figure 3. The lowest gaps between the dynamic defect states and the band edge are 0.02 and 0.16 eV for I_i and Cs_I respectively. It should be noted that the 0.16 eV gap between the Cs_I defect state and the CBM decreases to 0.06 eV in our HSE + SOC simulation. These values are comparable to k_BT which is about 0.03 eV at room temperature. Therefore, a significant thermal detrapping probability is expected for both dynamic defects at ambient conditions, helping to retain the carrier mobility.

The critical bottleneck of the all-inorganic perovskites lies in the bandgap. The covalent defects can introduce defect levels within the bandgap. As we have shown above, these dynamic defect levels will not be notably harmful to the carrier lifetime. Moreover, by decreasing the bandgap and fluctuating over a broad energy range, the dynamic defects will extend the absorbance into the red region of the solar spectrum.

Dynamic Defect Enhanced Sub-Bandgap Light Absorption. To characterize the gain of sub-bandgap light-harvesting induced by the dynamic defect levels, we compute the absorption spectra of the pristine $CsPbI_3$ and Cs_I systems by calculating and ensemble-averaging the transition dipole moments within the Franck−Condon approximation. Figure 5 shows that pristine $CsPbI_3$ possesses an excellent cross-bandgap absorption, similar to other MHPs.[55,56] The above bandgap absorption strength increases exponentially. The exponential Urbach band tail[57] just below the bandgap is from absorption induced by thermal phonon fluctuations.[58,59] However, sub-bandgap absorption is very limited in pristine $CsPbI_3$. Figure 5b shows that the Cs_I system possesses a notable defect-related sub-bandgap light absorption below 1.8 eV. The sub-bandgap absorption discussed here excludes multiphoton absorption.[60,61] Here, we emphasize that dynamic defect-induced photoabsorption can not be described in a static picture associated with the optimized system geometry corresponding to 0 K. The flat absorption terrace below the bandgap in Cs_I is induced by the time-averaged optical transition from the valence band to the dynamic defect level. The sub-bandgap absorption extends to 1.2 eV below the bandgap, which is in line with the amplitude of the dynamic defect level fluctuation in Figure 2d. The sub-bandgap absorption strength is weaker than the above-bandgap absorption, rationalized by the low defect DOS, as shown in Figure 2d. The gain of the sub-bandgap absorption is proportional to defect concentration. Here, we propose that an iodine-rich environment during the $CsPbI_3$ synthesis is likely to be beneficial for creating these dynamic defects and enhancing the sub-bandgap absorption. Sub-bandgap photo-currents generated by deep defect states are revealed in MHP-based photovoltaic devices.[59]

■ DISCUSSION AND CONCLUSIONS

The use of an IB or levels lying within the bandgap of a semiconductor has been proposed by Luque and Marti.[35] The IB increases PCE in light-harvesting via a sequence of two sub-bandgap optical excitation processes, in which one photon stimulates an electron from the VB to the IB (process 4 in Figure 3b,c) and another stimulates an electron from the IB to the CB (process 4 in Figure 3b,c), rising photocurrent and

preserving high voltage.[62,63] Notably, the IB solar cells can exceed the single gap solar cell efficiency limit by around 50% under one sun illumination.[64] There are various ways to realize an IB, such as high concentrations of impurities,[65] hetero-interfaces,[66] and quantum dot.[67] Nevertheless, so far, no technical implementations have benefited from the IB concept.[68] The bottleneck of IB solar cells is low photon absorption and high NA coupling between IBs and band edge states. Although most IBs enhance photon absorption, the IBs assisted nonradiative charge recombination is also significantly enhanced. The proposed general concept of dynamic defect is a promising solution to overcome the current bottleneck in IBs, since dynamic defects extend photoabsorption and preserve low nonradiative recombination, conferring the dynamic defect concept with a great potential as a novel absorber of future IB solar cells. Recent experiments have demonstrated efficient energy upconversion of up to 220 meV in MHPs, exceeding the thermal energy by nearly an order of magnitude.[69] It is feasible that defects contribute to the observed phenomenon.

To conclude, we demonstrated a new mechanism to enhance sub-bandgap photon harvesting and energy upconversion by novel covalent defect engineering with a suppressed nonradiative energy loss. Taking α-CsPbI$_3$ as a prototype, we have investigated the *e-h* recombination dynamics of the pristine system and in the presence of native point-defects using state-of-the-art ab initio quantum dynamics simulation. First, the energy levels of dynamic defects fluctuate significantly between shallow and deep states at ambient conditions, because thermal phonons significantly influence the electronic structure. Second, although the electronic properties associated with the defect states are distinct in these systems, we have not observed notable acceleration of charge recombination, even for the deep defects. Our analyses show that the strong defect tolerance in α-CsPbI$_3$ is due to the softness of the inorganic lattice and its low-frequency anharmonic phonons. For defects, the coordination of lattice deformation and strong covalent bonds significantly reduce the overlap between the trapped and free charges involved in the recombination, preventing the defects from acting as efficient charge recombination centers. Third, the deep levels can act as IBs for effective sub-bandgap absorption, which allows absorbing two sub-bandgap phonons sequentially. Sub-bandgap absorption assisted by IBs raises photocurrent and preserves high voltage.[67] In addition, the dynamic nature of the defect level facilitates light absorption over a broad energy range. The long lifetime of the trapped carriers is also beneficial to optical absorption from the IB to the main bands. Fourthly, we establish that both optical and thermal excitation are efficient pathways for carriers detrapping from the trap states to the band edges and enhancing their mobility. Finally, we propose that with proper control of the defect-induced *e-h* recombination, the IBs arising from the dynamic defects can help to exceed the SQ efficiency limit and achieve defect-mediated upconversion of thermal energy to current. We suggest that the established features of the dynamic defects are applicable to MHPs in general and possibly to other classes of materials.

METHODS

We employ ab initio NAMD simulations to calculate the nonradiative *e-h* recombination in the presence of the defects. The ab initio NAMD simulations are performed using the Hefei-NAMD code[70] within the real-time time-dependent density functional theory framework.[71] We use VASP[72−74] to optimize the structure, obtain room temperature (300 K) nuclear trajectories, and extract the Kohn−Sham orbitals that are needed to compute the NAC for the NAMD simulations. A $2 \times 2 \times 2$ supercell of α phase CsPbI$_3$ is employed. Additionally, a larger $2\sqrt{2} \times 2\sqrt{2} \times 4$ supercell is utilized to assess finite-size effects. The Perdew−Burke−Ernzerhof (PBE) exchange-correlation functional[75] is employed for the majority of the calculations. To validate the proposed dynamic defect, we also employ the Heyd−Scuseria−Ernzerhof (HSE06) functional,[74] incorporating spin−orbit coupling effects. We use a $3 \times 3 \times 1$ *k*-point mesh to sample the Brillouin zone in the geometry optimization, MD, and static calculations, while the *G*-point is used to perform NAMD. The NAC is calculated using the CAnac code with phase correction.[76−78] The absorption spectra are calculated using the standard expression for the oscillator strength that depends on the transition dipole moment and transition energy, shown in the Supporting Information. It is important to note that the defect concentration accessible in ab initio NAMD calculations is typically higher than in experiments. In order to reduce the defect density, one can employ machine learning based calculations[79] or scaling laws.[80]

ASSOCIATED CONTENT

Supporting Information

The Supporting Information is available free of charge at https://pubs.acs.org/doi/10.1021/acs.chemmater.4c02530.

Calculation of absorption spectrum; evolution of the CsI defect level obtained with a hybrid functional including spin−orbit coupling, and in a larger simulation cell; charge densities of band edge and defect levels; electron-vibrational influence spectra (PDF)

AUTHOR INFORMATION

Corresponding Authors

Weibin Chu − *Key Laboratory of Computational Physical Sciences (Ministry of Education), Institute of Computational Physical Sciences, Fudan University, Shanghai 200433, China; Department of Chemistry, University of Southern California, Los Angeles, California 90089, United States;* orcid.org/0000-0001-5951-0337; Email: wbchu@fudan.edu.cn

Oleg V. Prezhdo − *Department of Chemistry, University of Southern California, Los Angeles, California 90089, United States; Department of Physics and Astronomy, University of Southern California, Los Angeles, California 90089, United States;* orcid.org/0000-0002-5140-7500; Email: prezhdo@usc.edu

Authors

Yongliang Shi − *State Key Laboratory of Surface Physics and Department of Physics, Fudan University, Shanghai 200433, China; Center for Spintronics and Quantum Systems, State Key Laboratory for Mechanical Behavior of Materials, School of Materials Science and Engineering, Xi'an Jiaotong University, Xi'an, Shaanxi 710049, China*

Lili Zhang − *Key Laboratory of Material Physics, Ministry of Education, School of Physics and Microelectronics, Zhengzhou University, Zhengzhou 450001, China;* orcid.org/0000-0001-9243-7960

Bipeng Wang − *Department of Chemical Engineering, University of Southern California, Los Angeles, California 90089, United States;* orcid.org/0000-0003-0924-5867

Wissam A. Saidi − *National Energy Technology Laboratory, Pittsburgh, Pennsylvania 15236, United States; Department of Mechanical Engineering and Materials Science, University*

of Pittsburgh, Pittsburgh, Pennsylvania 15261, United States; orcid.org/0000-0001-6714-4832

Jin Zhao − Department of Physics and ICQD/Hefei National Research Center for Physical Sciences at the Microscale, University of Science and Technology of China, Hefei, Anhui 230026, China; orcid.org/0000-0003-1346-5280

Complete contact information is available at:
https://pubs.acs.org/10.1021/acs.chemmater.4c02530

Notes

The authors declare no competing financial interest.

■ REFERENCES

(1) Kojima, A.; Teshima, K.; Shirai, Y.; Miyasaka, T. Organometal Halide Perovskites as Visible-Light Sensitizers for Photovoltaic Cells. J. Am. Chem. Soc. 2009, 131 (17), 6050−6051.

(2) Chi, W. G.; Banerjee, S. K. Achieving Resistance against Moisture and Oxygen for Perovskite Solar Cells with High Efficiency and Stability. Chem. Mater. 2021, 33 (12), 4269−4303.

(3) Zhu, H.; Miyata, K.; Fu, Y.; Wang, J.; Joshi, P. P.; Niesner, D.; Williams, K. W.; Jin, S.; Zhu, X.-Y. Screening in crystalline liquids protects energetic carriers in hybrid perovskites. Science 2016, 353 (6306), 1409−1413.

(4) Jena, A. K.; Kulkarni, A.; Miyasaka, T. Halide Perovskite Photovoltaics: Background, Status, and Future Prospects. Chem. Rev. 2019, 119 (5), 3036−3103.

(5) Aebli, M.; Porenta, N.; Aregger, N.; Kovalenko, M. V. Local Structure of Multinary Hybrid Lead Halide Perovskites Investigated by Nuclear Quadrupole Resonance Spectroscopy. Chem. Mater. 2021, 33 (17), 6965−6973.

(6) Park, S. M.; Wei, M. Y.; Xu, J.; Atapattu, H. R.; Eickemeyer, F. T.; Darabi, K.; Grater, L.; Yang, Y.; Liu, C.; Teale, S.; et al. Engineering ligand reactivity enables high-temperature operation of stable perovskite solar cells. Science 2023, 381 (6654), 209−215.

(7) Wang, F.; Fu, Y.; Ziffer, M. E.; Dai, Y.; Maehrlein, S. F.; Zhu, X. Y. Solvated Electrons in Solids-Ferroelectric Large Polarons in Lead Halide Perovskites. J. Am. Chem. Soc. 2021, 143 (1), 5−16.

(8) Yan, J. K.; Li, H. J.; Aldamasy, M. H.; Frasca, C.; Abate, A.; Zhao, K.; Hu, Y. Advances in the Synthesis of Halide Perovskite Single Crystals for Optoelectronic Applications. Chem. Mater. 2023, 35, 2683−2712.

(9) Karlsson, M.; Yi, Z. Y.; Reichert, S.; Luo, X. Y.; Lin, W. H.; Zhang, Z. Y.; Bao, C. X.; Zhang, R.; Bai, S.; Zheng, G. H. J.; et al. Mixed halide perovskites for spectrally stable and high-efficiency blue light-emitting diodes. Nat. Commun. 2021, 12 (1), No. 361, DOI: 10.1038/s41467-020-20582-6.

(10) Bai, S.; Da, P.; Li, C.; Wang, Z.; Yuan, Z.; Fu, F.; Kawecki, M.; Liu, X.; Sakai, N.; Wang, J. T.-W.; et al. Planar perovskite solar cells with long-term stability using ionic liquid additives. Nature 2019, 571 (7764), 245−250.

(11) Min, H.; Kim, M.; Lee, S.-U.; Kim, H.; Kim, G.; Choi, K.; Lee, J. H.; Seok, S. I. Efficient, stable solar cells by using inherent bandgap

(12) Wang, Y.; Dar, M. I.; Ono, L. K.; Zhang, T.; Kan, M.; Li, Y.; Zhang, L.; Wang, X.; Yang, Y.; Gao, X.; et al. Thermodynamically stabilized beta-CsPbI3-based perovskite solar cells with efficiencies > 18%. Science 2019, 365 (6453), 591−595.

of α-phase formamidinium lead iodide. Science 2019, 366 (6466), 749−753.

(13) National Renewable Energy Laboratory (NREL) https://www.nrel.gov/pv/cell-efficiency.html/. (accessed December 21, 2024).

(14) Raval, P.; Kazemi, M. A. A.; Ruellou, J.; Trebosc, J.; Lafon, O.; Delevoye, L.; Sauvage, F.; Reddy, G. N. M. Examining a Year-Long Chemical Degradation Process and Reaction Kinetics in Pristine and Defect-Passivated Lead Halide Perovskites. Chem. Mater. 2023, 35, 2904−2917, DOI: 10.1021/acs.chemmater.2c03803.

(15) Juarez-Perez, E. J.; Hawash, Z.; Raga, S. R.; Ono, L. K.; Qi, Y. Thermal degradation of CH3NH3PbI3 perovskite into NH3 and CH3I gases observed by coupled thermogravimetry-mass spectrometry analysis. Energy Environ. Sci. 2016, 9 (11), 3406−3410.

(16) Boyd, C. C.; Cheacharoen, R.; Leijtens, T.; McGehee, M. D. Understanding Degradation Mechanisms and Improving Stability of Perovskite Photovoltaics. Chem. Rev. 2019, 119 (5), 3418−3451.

(17) Roy, B.; Mahato, S.; Bose, S.; Ghorai, A.; Srivastava, S. K.; Das, N. C.; Ray, S. K. Cu-Doping Induced Phase Transformation in CsPbI3 Nanocrystals with Enhanced Structural Stability and Photoluminescence Quantum Yield. Chem. Mater. 2023, 35 (4), 1601−1609.

(18) Kim, D.; Ryu, H.; Lim, S. Y.; McCall, K. M.; Park, J.; Kim, S.; Kim, T. J.; Kim, J.; Kim, Y. S.; Kanatzidis, M. G.; et al. On the Origin of Room-Temperature Amplified Spontaneous Emission in CsPbBr3 Single Crystals. Chem. Mater. 2021, 33 (18), 7185−7193.

(19) Wang, Y.; Zhang, T.; Kan, M.; Zhao, Y. Bifunctional Stabilization of All-Inorganic alpha-CsPbI3 Perovskite for 17% Efficiency Photovoltaics. J. Am. Chem. Soc. 2018, 140 (39), 12345−12348.

(20) Kulbak, M.; Cahen, D.; Hodes, G. How Important Is the Organic Part of Lead Halide Perovskite Photovoltaic Cells? Efficient CsPbBr3 Cells. J. Phys. Chem. Lett. 2015, 6 (13), 2452−2456.

(21) Mishra, A.; DiLuzio, S.; Alahbakhshi, M.; Adams, A. C.; Bowler, M. H.; Moon, J.; Gu, Q.; Zakhidov, A. A.; Bernhard, S.; Slinker, J. D. Bright Single-Layer Perovskite Host-Ionic Guest Light-Emitting Electrochemical Cells. Chem. Mater. 2021, 33 (4), 1201−1212.

(22) Stelmakh, A.; Aebli, M.; Baumketner, A.; Kovalenko, M. V. On the Mechanism of Alkylammonium Ligands Binding to the Surface of CsPbBr333333333 Nanocrystals. Chem. Mater. 2021, 33 (15), 5962−5973.

(23) Zhao, W.; Su, R.; Huang, Y.; Wu, J.; Fong, C. F.; Feng, J.; Xiong, Q. Transient circular dichroism and exciton spin dynamics in all-inorganic halide perovskites. Nat. Commun. 2020, 11 (1), No. 5665.

(24) Liu, X.; Wang, X.; Zhang, T.; Miao, Y.; Qin, Z.; Chen, Y.; Zhao, Y. Organic Tetrabutylammonium Cation Intercalation to Heal Inorganic CsPbI3 Perovskite. Angew. Chem., Int. Ed. 2021, 60, 12351−12355.

(25) Wang, Y.; Chen, G.; Ouyang, D.; He, X.; Li, C.; Ma, R.; Yin, W.-J.; Choy, W. C. H. High Phase Stability in CsPbI3 Enabled by Pb-I Octahedra Anchors for Efficient Inorganic Perovskite Photovoltaics. Adv. Mater. 2020, 32 (24), No. 2000186.

(26) Wang, Y.; Liu, X. M.; Zhang, T. Y.; Wang, X. T.; Kan, M.; Shi, J. L.; Zhao, Y. X. The Role of Dimethylammonium Iodide in CsPbI3 Perovskite Fabrication: Additive or Dopant? Angew. Chem., Int. Ed. 2019, 58 (46), 16691−16696.

(27) Shockley, W.; Queisser, H. J. Detailed Balance Limit of efficiency of P-N junction solar cells. J. Appl. Phys. 1961, 32 (3), 510−519.

(28) Faheem, M. B.; Khan, B.; Feng, C.; Farooq, M. U.; Raziq, F.; Xiao, Y.; Li, Y. All-Inorganic Perovskite Solar Cells: Energetics, Key Challenges, and Strategies toward Commercialization. ACS Energy Lett. 2020, 5 (1), 290−320.

(29) Shockley, W.; Read, W. T. Statistics of the recombinations of holes and electrons. Phys. Rev. 1952, 87 (5), No. 835.

(30) Chu, W.; Saidi, W. A.; Zhao, J.; Prezhdo, O. V. Soft Lattice and Defect Covalency Rationalize Tolerance of beta-CsPbI3 Perovskite Solar Cells to Native Defects. *Angew. Chem., Int. Ed.* **2020**, *59* (16), 6435−6441.

(31) Chu, W.; Zheng, Q.; Prezhdo, O. V.; Zhao, J.; Saidi, W. A. Low-frequency lattice phonons in halide perovskites explain high defect tolerance toward electron-hole recombination. *Sci. Adv.* **2020**, *6* (7), No. eaaw7453.

(32) Li, W.; She, Y. L.; Vasenko, A. S.; Prezhdo, O. V. Ab initio nonadiabatic molecular dynamics of charge carriers in metal halide perovskites. *Nanoscale* **2021**, *13* (23), 10239−10265.

(33) Ma, X. B.; Fang, W. H.; Long, R.; Prezhdo, O. V. Compression of Organic Molecules Coupled with Hydrogen Bonding Extends the Charge Carrier Lifetime in BA2SnI4. *J. Am. Chem. Soc.* **2024**, *146* (23), 16314−16323.

(34) Zhao, X.; Vasenko, A. S.; Prezhdo, O. V.; Long, R. Anion Doping Delays Nonradiative Electron−Hole Recombination in Cs-Based All-Inorganic Perovskites: Time Domain ab Initio Analysis. *J. Phys. Chem. Lett.* **2022**, *13* (49), 11375−11382.

(35) Luque, A.; Martí, A. Increasing the Efficiency of Ideal Solar Cells by Photon Induced Transitions at Intermediate Levels. *Phys. Rev. Lett.* **1997**, *78* (26), No. 5014.

(36) Sutton, R. J.; Filip, M. R.; Haghighirad, A. A.; Sakai, N.; Wenger, B.; Giustino, F.; Snaith, H. J. Cubic or Orthorhombic? Revealing the Crystal Structure of Metastable Black-Phase CsPbI333333333 by Theory and Experiment. *ACS Energy Lett.* **2018**, *3* (8), 1787−1794.

(37) Wang, C. J.; Chesman, A. S. R.; Jasieniak, J. J. Stabilizing the cubic perovskite phase of CsPbI3 nanocrystals by using an alkyl phosphinic acid. *Chem. Commun.* **2017**, *53* (1), 232−235.

(38) Liang, J.; Han, X.; Yang, J. H.; Zhang, B. Y.; Fang, Q. Y.; Zhang, J.; Ai, Q.; Ogle, M. M.; Terlier, T.; Marti, A. A.; Lou, J. Defect-Engineering-Enabled High-Efficiency All-Inorganic Perovskite Solar Cells. *Adv. Mater.* **2019**, *31* (51), No. 1903448.

(39) Huang, Y.; Yin, W.-J.; He, Y. Intrinsic Point Defects in Inorganic Cesium Lead Iodide Perovskite CsPbI3. *J. Phys. Chem. C* **2018**, *122* (2), 1345−1350.

(40) Shan, W. T.; Saidi, W. A. Segregation of Native Defects to the Grain Boundaries in Methylammonium Lead Iodide Perovskite. *J. Phys. Chem. Lett.* **2017**, *8* (23), 5935−5942.

(41) Yin, W. J.; Shi, T. T.; Yan, Y. F. Unusual defect physics in CH3NH3PbI3 perovskite solar cell absorber. *Appl. Phys. Lett.* **2014**, *104* (6), No. 063903.

(42) Mosconi, E.; Quarti, C.; Ivanovska, T.; Ruani, G.; De Angelis, F. Structural and electronic properties of organo-halide lead perovskites: a combined IR-spectroscopy and ab initio molecular dynamics investigation. *Phys. Chem. Chem. Phys.* **2014**, *16* (30), 16137−16144.

(43) Agiorgousis, M. L.; Sun, Y. Y.; Zeng, H.; Zhang, S. B. Strong Covalency-Induced Recombination Centers in Perovskite Solar Cell Material CH(3)NH(3)PbI(3). *J. Am. Chem. Soc.* **2014**, *136* (41), 14570−14575.

(44) Marronnier, A.; Lee, H.; Geffroy, B.; Even, J.; Bonnassieux, Y.; Roma, G. Structural Instabilities Related to Highly Anharmonic Phonons in Halide Perovskites. *J. Phys. Chem. Lett.* **2017**, *8* (12), 2659−2665.

(45) Jaeger, H. M.; Fischer, S.; Prezhdo, O. V. Decoherence-induced surface hopping. *J. Chem. Phys.* **2012**, *137* (22), No. 22A545.

(46) Liu, D. Y.; Wang, B. P.; Vasenko, A. S.; Prezhdo, O. V. Decoherence ensures convergence of non-adiabatic molecular dynamics with number of states. *J. Chem. Phys.* **2024**, *161* (6), No. 064104.

(47) Akimov, A. V.; Prezhdo, O. V. The PYXAID Program for Non-Adiabatic Molecular Dynamics in Condensed Matter Systems. *J. Chem. Theory Comput.* **2013**, *9* (11), 4959−4972.

(48) Zheng, Q.; Chu, W.; Zhao, C.; Zhang, L.; Guo, H.; Wang, Y.; Jiang, X.; Zhao, J. Ab initio nonadiabatic molecular dynamics investigations on the excited carriers in condensed matter systems. *WIREs Comput. Mol. Sci.* **2019**, *9* (6), No. e1411.

(49) Akimov, A. V.; Prezhdo, O. V. Advanced Capabilities of the PYXAID Program: Integration Schemes, Decoherenc:e Effects, Multiexcitonic States, and Field-Matter Interaction. *J. Chem. Theory Comput.* **2014**, *10* (2), 789−804.

(50) Gumber, S.; Prezhdo, O. V. Zeno and Anti-Zeno Effects in Nonadiabatic Molecular Dynamics. *J. Phys. Chem. Lett.* **2023**, *14* (32), 7274−7282.

(51) Zhang, L.; Wang, Q.; Wang, L.; Wang, L.; Zhao, J.; Li, S. Ultrafast charge transfer in anisotropic black phosphorus/${\mathrm{TiS}}_{3}$ heterostructures for photoconversion. *Phys. Rev. B* **2024**, *109* (7), No. 075306.

(52) Kamisaka, H.; Kilina, S. V.; Yamashita, K.; Prezhdo, O. V. Ultrafast vibrationally-induced dephasing of electronic excitations in PbSe quantum dot. *Nano Lett.* **2006**, *6* (10), 2295−2300.

(53) Myung, C. W.; Yun, J.; Lee, G.; Kim, K. S. A New Perspective on the Role of A-Site Cations in Perovskite Solar Cells. *Adv. Energy Mater.* **2018**, *8* (14), No. 1702898, DOI: 10.1002/aenm.201702898.

(54) Ni, Z.; Bao, C.; Liu, Y.; Jiang, Q.; Wu, W.-Q.; Chen, S.; Dai, X.; Chen, B.; Hartweg, B.; Yu, Z.; et al. Resolving spatial and energetic distributions of trap states in metal halide perovskite solar cells. *Science* **2020**, *367* (6484), 1352−1358.

(55) Yin, W.-J.; Shi, T.; Yan, Y. Unique Properties of Halide Perovskites as Possible Origins of the Superior Solar Cell Performance. *Adv. Mater.* **2014**, *26* (27), 4653−4658.

(56) Grancini, G.; Marras, S.; Prato, M.; Giannini, C.; Quarti, C.; De Angelis, F.; De Bastiani, M.; Eperon, G. E.; Snaith, H. J.; Manna, L.; Petrozza, A. The Impact of the Crystallization Processes on the Structural and Optical Properties of Hybrid Perovskite Films for Photovoltaics. *J. Phys. Chem. Lett.* **2014**, *5* (21), 3836−3842.

(57) Urbach, F. The Long-Wavelength Edge of Photographic Sensitivity and of the Electronic Absorption of Solids. *Phys. Rev.* **1953**, *92* (5), No. 1324.

(58) Caselli, V. M.; Wei, Z.; Ackermans, M. M.; Hutter, E. M.; Ehrler, B.; Savenije, T. J. Charge Carrier Dynamics upon Sub-bandgap Excitation in Methylammonium Lead Iodide Thin Films: Effects of Urbach Tail, Deep Defects, and Two-Photon Absorption. *ACS Energy Lett.* **2020**, *5* (12), 3821−3827.

(59) Sutter-Fella, C. M.; Miller, D. W.; Ngo, Q. P.; Roe, E. T.; Toma, F. M.; Sharp, I. D.; Lonergan, M. C.; Javey, A. Band Tailing and Deep Defect States in CH3NH3Pb(I1-xBrx)(3) Perovskites As Revealed by Sub-Bandgap Photocurrent. *ACS Energy Lett.* **2017**, *2* (3), 709−715.

(60) Wei, Z.; Guo, D.; Thieme, J.; Katan, C.; Caselli, V. M.; Even, J.; Savenije, T. J. The importance of relativistic effects on two-photon absorption spectra in metal halide perovskites. *Nat. Commun.* **2019**, *10* (1), No. 5342.

(61) Krishnakanth, K. N.; Seth, S.; Samanta, A.; Rao, S. V. Broadband ultrafast nonlinear optical studies revealing exciting multi-photon absorption coefficients in phase pure zero-dimensional Cs4PbBr6 perovskite films. *Nanoscale* **2019**, *11* (3), 945−954.

(62) Mellor, A.; Luque, A.; Tobias, I.; Marti, A. Realistic Detailed Balance Study of the Quantum Effi ciency of Quantum Dot Solar Cells. *Adv. Funct. Mater.* **2014**, *24* (3), 339−345.

(63) Hosokawa, H.; Tamaki, R.; Sawada, T.; Okonogi, A.; Sato, H.; Ogomi, Y.; Hayase, S.; Okada, Y.; Yano, T. Solution-processed intermediate-band solar cells with lead sulfide quantum dots and lead halide perovskites. *Nat. Commun.* **2019**, *10*, No. 43, DOI: 10.1038/s41467-018-07655-3.

(64) Krishna, A.; Krich, J. J. Increasing efficiency in intermediate band solar cells with overlapping absorptions. *J. Opt.* **2016**, *18* (7), No. 074010.

(65) Luque, A.; Martí, A.; Antolín, E.; Tablero, C. Intermediate bands versus levels in non-radiative recombination. *Phys. B* **2006**, *382* (1), 320−327.

(66) Asahi, S.; Teranishi, H.; Kusaki, K.; Kaizu, T.; Kita, T. Two-step photon up-conversion solar cells. *Nat. Commun.* **2017**, *8*, No. 14962, DOI: 10.1038/ncomms14962.

(67) Ramiro, I.; Villa, J.; Hwang, J.; Martin, A. J.; Millunchick, J.; Phillips, J.; Marti, A. Demonstration of a GaSb/GaAs Quantum Dot

Intermediate Band Solar Cell Operating at Maximum Power Point. *Phys. Rev. Lett.* **2020**, *125* (24), No. 247703, DOI: 10.1103/PhysRevLett.125.247703.

(68) Ramiro, I.; Marti, A. Intermediate band solar cells: Present and future. *Prog. Photovoltaics* **2021**, *29*, 705−713.

(69) Wu, B.; Wang, A. C.; Fu, J.; Zhang, Y. T.; Yang, C.; Gong, Y. Y.; Jiang, C. X.; Long, M. Z.; Zhou, G. F.; Yue, S.; et al. Uncovering the mechanisms of efficient upconversion in two-dimensional perovskites with anti-Stokes shift up to 220 meV. *Sci. Adv.* **2023**, *9* (39), No. eadi9347, DOI: 10.1126/sciadv.adi9347.

(70) Zheng, Q.; Chu, W.; Zhao, C.; Zhang, L.; Guo, H.; Wang, Y.; Jiang, X.; Zhao, J. Ab initio nonadiabatic molecular dynamics investigations on the excited carriers in condensed matter systems. *WIREs Comput. Mol. Sci.* **2019**, *9* (6), No. e1411, DOI: 10.1002/wcms.1411.

(71) Craig, C. F.; Duncan, W. R.; Prezhdo, O. V. Trajectory surface hopping in the time-dependent Kohn-Sham approach for electron-nuclear dynamics. *Phys. Rev. Lett.* **2005**, *95* (16), No. 163001, DOI: 10.1103/PhysRevLett.95.163001.

(72) Kresse, G.; Hafner, J. Ab-Initio Molecular-Dynamics Simulation of the Liquid-Metal Amorphos-Semiconductor Transition in Germanium. *Phys. Rev. B* **1994**, *49* (20), No. 14251.

(73) Kresse, G.; Hafner, J. Ab initio molecular dynamics for liquid metals. *Phys. Rev. B* **1993**, *47* (1), No. 558.

(74) Kresse, G.; Hafner, J. Ab initiomolecular dynamics for open-shell transition metals. *Phys. Rev. B* **1993**, *48* (17), No. 13115.

(75) Kresse, G.; Joubert, D. From ultrasoft pseudopotentials to the projector augmented-wave method. *Phys. Rev. B* **1999**, *59* (3), No. 1758.

(76) Chu, W.; Prezhdo, O. V. Concentric Approximation for Fast and Accurate Numerical Evaluation of Nonadiabatic Coupling with Projector Augmented-Wave Pseudopotentials. *J. Phys. Chem. Lett.* **2021**, *12* (12), 3082−3089.

(77) Akimov, A. V. A Simple Phase Correction Makes a Big Difference in Nonadiabatic Molecular Dynamics. *J. Phys. Chem. Lett.* **2018**, *9* (20), 6096−6102.

(78) Chu, W.; Zheng, Q.; Akimov, A. V.; Zhao, J.; Saidi, W. A.; Prezhdo, O. V. Accurate Computation of Nonadiabatic Coupling with Projector Augmented-Wave Pseudopotentials. *J. Phys. Chem. Lett.* **2020**, *11* (23), 10073−10080.

(79) Liu, D. Y.; Wang, B. P.; Wu, Y. F.; Vasenko, A. S.; Prezhdo, O. V. Breaking the size limitation of nonadiabatic molecular dynamics in condensed matter systems with local descriptor machine learning. *Proc. Natl. Acad. Sci. U.S.A.* **2024**, *121*, No. e2403497121.

(80) Wang, S. S.; Huang, M. L.; Wu, Y. N.; Chu, W. B.; Zhao, J.; Walsh, A.; Gong, X. G.; Wei, S. H.; Chen, S. Y. Effective lifetime of non-equilibrium carriers in semiconductors from non-adiabatic molecular dynamics simulations. *Nat. Comput. Sci.* **2022**, *2* (8), 486−493.